

## Track your satellite before it is too late: a laser ranging enabled student CubeSat project

**Luca Lion<sup>a</sup>\*, Federico Basana<sup>a</sup>, Mattia Sambo<sup>b</sup>, Savina Tsichili<sup>b</sup>, Alessandro Francesconi<sup>c</sup>**

<sup>a</sup>*Centre of Studies and Activities for Space (CISAS) "Giuseppe Colombo", University of Padova, via Venezia, 15, Padova, 35131, Italy*

<sup>b</sup>*University of Padova, Via Venezia, 1, Padova, 35131, Italy*

<sup>c</sup>*Department of Industrial Engineering, University of Padova, Via Venezia, 1, Padova, 35131, Italy*

### Abstract

The proliferation of small satellites orbiting the Earth marks an exciting era in space exploration, offering greater opportunities for students and academic institutions to get involved. However, this increase in the number of satellites also raises serious concerns, particularly regarding the growing problem of space debris in low Earth orbit (LEO). With over 3000 Resident Space Objects (RSOs) larger than 10 cm and an estimated 120 million smaller fragments, the risk to operational spacecraft and future missions is significant, requiring innovative solutions for debris management and satellite tracking. In the midst of these challenges, the AlbaSat mission aims to improve the capabilities of small satellites through the integration of laser ranging tracking systems. The mission is currently under development at the University of Padova by the Alba CubeSat UniPD student team. The satellite incorporates commercial off-the-shelf (COTS) Corner Cube Retroreflectors (CCRs) on three of its six faces, carefully designed to minimise interference with other subsystems and components. Simple, off-the-shelf solar panels and other payload positioning guide the placement of the CCRs, reducing the complexity of the system. The satellite hosts three types of corner cubes on board: an uncoated 12.7mm, an aluminium-coated 12.7mm and a 25.4mm uncoated Active Modulated Retro Reflector, which is recycled as a standard CCR when not in use by another payload of the mission. This variety of CCRs enables accurate orbit determination by laser ranging and basic attitude determination by identifying the specific face illuminated by the laser, thereby improving the quantity and quality of information available from ground laser observations. This paper outlines the development process, including feasibility studies and link budget analyses, carried out to ensure optimal system performance under real-world conditions. Advanced simulation tools such as IOTA (In-Orbit Tumbling Analysis), developed by Hyperschall Technologie Goettingen GmbH under an ESA contract in 2022, were used to model satellite tumbling dynamics and simulate laser ranging measurements to refine the tracking system's operational parameters. The AlbaSat mission represents a collaborative effort to advance small satellite technology. Following the successful completion of ESA's Fly Your Satellite! Design Booster programme, the mission is progressing towards the Critical Design Review and is poised to make a practical and impactful contribution to satellite tracking capabilities and space debris mitigation efforts. The reconstruction is confronted with the original CAD model used to create the synthetic images.

**Keywords:** Space Debris, Inspection, CubeSat, Photogrammetry, Computer Vision.

### 1. Introduction

The risk of space debris is a growing concern as the number of objects in Earth's orbit continues to increase. Space debris, also known as "space junk," includes defunct satellites, spent rocket stages, and fragments resulting from collisions. These objects, ranging from large pieces of abandoned spacecraft to tiny paint flecks, pose significant hazards to operational satellites, the International Space Station (ISS), and future space missions. As of 2024, there are more than 30,000 trackable objects in Earth's orbit, and estimates suggest that there are over 100 million pieces of debris smaller than 1 centimetre. Even these small fragments can cause severe damage due to the

high relative velocities in orbit, which can exceed 28,000 kilometres per hour. The increasing density of debris in low Earth orbit (LEO) raises the risk of collisions, which can create even more debris in a cascading effect known as the Kessler syndrome. This scenario could lead to a runaway chain reaction of collisions, significantly increasing the amount of debris and making certain orbital regions unusable. The importance of debris tracking goes beyond avoiding collisions with operational satellites. It is also essential for the long-term sustainability of space activities. As more countries and private companies launch satellites, especially with the rise of megaconstellations like Starlink, the need for effective debris tracking becomes even more critical. Without adequate tracking and mitigation measures, increasing orbital congestion could

lead to more frequent collisions, threatening the viability of space exploration and exploitation for future generations. Satellite laser ranging (SLR) has established itself as a pivotal technology in modern geodesy and space situational awareness, providing unmatched precision in the positioning of satellites and contributing significantly to space traffic management and debris mitigation [1]. By measuring the round-trip time of a laser pulse emitted from ground stations to satellites equipped with retroreflectors, SLR achieves centimeter-level accuracy in orbit determination, a capability essential for various applications, including global navigation satellite systems (GNSS) like GPS, Galileo, and BeiDou. The evolution of SLR has expanded its utility across different orbital regimes, from low Earth orbit (LEO) to geosynchronous orbit (GEO), ensuring that it remains a key tool in maintaining the operational integrity of these satellites. The integration of SLR with microwave-based GNSS tracking enhances the accuracy and reliability of positioning, navigation, and timing (PNT) services by leveraging the strengths of both technologies—SLR's precision in direct distance measurement and GNSS's continuous tracking capability. Despite these advancements, the rapid proliferation of small satellites and CubeSats, particularly in LEO, has introduced new challenges. The increasing number of objects in space has led to a significant rise in the density of satellites, escalating the risk of collisions and emphasizing the need for more sophisticated tracking and collision avoidance systems. As satellites reach the end of their operational life, they often transition into non-cooperative objects, no longer providing telemetry data and effectively becoming space debris. The ability to track these defunct satellites is crucial for preventing collisions with operational spacecraft and ensuring the long-term sustainability of space activities. Unlike traditional radio-based methods, which rely on active signals from the satellite, SLR can track these non-cooperative objects based purely on their physical presence in space, provided they are equipped with retroreflectors. This capability is especially relevant in the context of the AlbaSat mission, which incorporates commercial off-the-shelf (COTS) Corner Cube Retroreflectors (CCRs) on multiple faces of the satellite. These CCRs enable precise laser ranging and orbit determination both during the satellite's operational life and after its decommissioning, ensuring continued tracking even as it transitions into a debris object. The AlbaSat mission not only enhances the tracking capabilities for small satellites but also represents a proactive approach to space debris mitigation. By ensuring that satellites remain trackable even after their mission ends, AlbaSat contributes to the safety and sustainability of space operations. This mission exemplifies how modern advancements in SLR and POD can be applied to address the growing challenges posed by the increasing density of space objects, ultimately supporting the broader goals of space situational awareness and debris management.

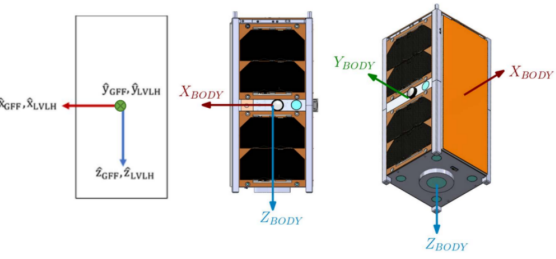


**Fig. 1.** LVLH & BODY reference system on Cubesat.

creasing density of space objects, ultimately supporting the broader goals of space situational awareness and debris management.

## 2. Analysis

### 2.1 System Structure

A Corner Cube Reflector is a specialized optical device designed to reflect an incoming light beam back to its source; it does so, with minimal scattering, regardless of the angle at which the beam strikes the reflector. CCRs consist of three mutually perpendicular, intersecting flat surfaces, forming a corner shape, similar to a corner of a cube. This geometric configuration ensures that light entering the CCR is reflected precisely back in the direction it came from. In this research, it is used for satellite laser ranging; ground-based stations emit laser pulses toward satellites equipped with CCRs, and the reflected signals are used to determine precise distances based on the time taken for the laser to return [2]. A total of three CCRs are mounted on the structures, with the aim of reflecting the laser beam coming from the selected ground stations for orbital determination. As reference systems, both the LVLH (Local Vertical, Local Horizontal) and BODY systems are considered. In the BODY system, the center of the three axes is positioned at the center of gravity of the satellite, while the whole system rotates in a motion perpendicular to the satellite itself (Fig. 1).

As for the LVLH system, the  $\hat{z}_{\text{LVLH}}$  axis is directed along the nadir direction, the  $\hat{y}_{\text{LVLH}}$  axis is in the opposite direction to the orbital angular momentum, and the  $\hat{x}_{\text{LVLH}}$  axis is orthogonal to the other two (Fig. 2).

Regarding their arrangement, each of them is placed on the +Y, -Y and +Z faces accordingly, as shown in Figure 1. For this analysis, spacecraft orbit is assumed to be affected by secular and periodic perturbations caused by Earth geometry and atmospheric drag. A nadir-pointing attitude with no error is assumed. The ground station is assumed to start pointing at the CCR immediately when it becomes visible, while tracking mount pointing errors are not considered. Table 1 describes CCR positioning and each CCR is assumed to be at the center of the face it is mounted on. The one on the +Z face will be used

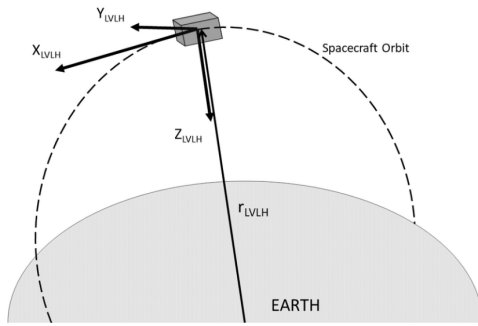


**Fig. 2.** Above, representation of the LVLH system.

CCR	Position
1	+Z face
2	+Y face
3	-Y face

**Table 1.** CCR positioning for orbital simulation.

when it is not occupied as a Modulating Retroreflector (MRR) by the Quantum Payload. At first, the initial

design consisted of 7 CCRs; 6 on the +Y and -Y faces, and the MRR on the +Z. However, the CCRs were redistributed and reduced to 4, to ensure better visibility in the tumbling case of the satellite. Finally, the current design consists of only 3 components; this is primarily due to incompatibility with the solar panels, space constraints with the Quantum Payload and due to velocity aberration, as well. The development process of the structure of the CCRs is shown in Figure 3. The velocity aberration effect causes the beam to be deflected by an amount  $\alpha = \frac{2v}{c}$  in the forward direction of the satellite motion, where  $v$  is the relative velocity between the satellite and station and  $c$  is the speed of light. If  $\alpha$  is large compared to the angular width of the retro FFDP (Far Field Diffraction Pattern), the reflected beam will not be seen by the SLR station. In fact, the already difficult task to individually identify the four different CCRs in the +Z was made impossible by the presence of the MRR positioned in the middle of the face, so the MRR will be kept “turned-on” when not operative, this way the MRR will act as standard CCR and can be used to perform Laser Ranging. The diameters of the three CCRs are 12.7mm ( $\pm$  Y faces) and 25.4mm (+Z face). The MRR and the CCR on +Y are uncoated while the one on the -Y is AR silver coated. They are all made of N-BK7 glass by Edmund Optics. The mounting configuration per each CCR is represented in Figure 4. The chosen adhesive used to glue the CCRs to the holding structure is 3M™ Scotch-Weld™ Epoxy Adhesive 2216 B/A, while the fastenings screws used to connect the holding structure to the satellite are M2.5 x 5mm countersunk head

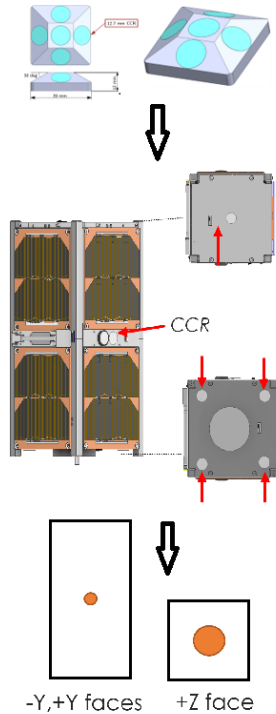


**Fig. 3.** CCRs’ design development process.

hexagon socket drive screws, from Trfastenings

## 2.2 Link Budget

First, there are two different ways of operating the SLR stations; the single-photon and the multi-photon regime. This aspect influences the recorded received photons from the station. Operating in a multi-photon regime would mean the system is designed to detect multiple photons simultaneously. This increases the likelihood of detecting background noise—such as sunlight or stray reflections—alongside the actual signal. Consequently, this increases the probability of false positives, where noise

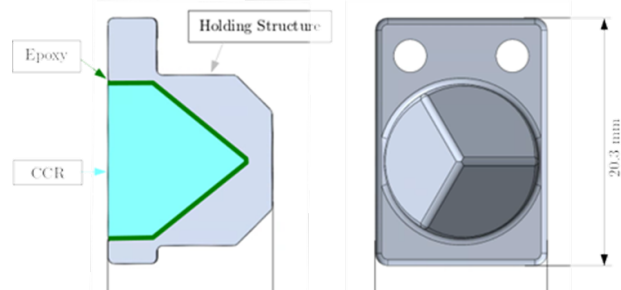


**Fig. 4.** CCR mounting system

is mistaken for the true signal. For this reason, single-photon detectors were chosen for this research, since the primary goal of the payload was higher-precision ranging. More specifically, this regime minimizes the risk of excessive noise by being more selective in what it detects, leading to cleaner measurements. Since only one photon is detected per pulse, it provides more sensitivity, an improved signal-to-noise ratio, more precise timing resolution—and so better distance measurements—and a higher dynamic range, being able to handle a wider range of photon fluxes. However, the detection signals are weaker which will be challenging for conditions with higher background noise and the data rate will be limited [3].

The link budget analysis aims to determine the efficiency and effectiveness of different CCR designs and configurations under various operational conditions. The approach involves using the laser link equation to calculate the mean number of photoelectrons received per transmitted laser pulse [4]. Specifically, the laser link equation provides an estimate of photon return based on laser energy, range, array cross section, optics efficiency and weather:

$$N_{pe} = \eta_q \left( \frac{E_T}{h\nu} \right) \eta_T G_T \sigma_{\text{eff}} \left( \frac{1}{4\pi R^2} \right)^2 A_R \eta_R T_A^2 T_c^2$$

where  $\eta_q$  is the quantum efficiency of the receiver,  $E_T$  is the laser pulse energy in mJ,  $h\nu$  is the photon energy ( $3.73 \cdot 10^{-19}$  J at 532 nm),  $\eta_T$  is the efficiency of the transmitting optics,  $G_T$  is the laser beam gain,  $\sigma_{\text{eff}}$  is the CCR optical cross section (OCS),  $R$  is the slant range to the target,  $A_R$  is the telescope aperture,  $\eta_R$  is the efficiency of the receiving optics,  $T_A$  is the one way atmospheric transmission, and  $T_c$  is the one way transmissivity of cirrus clouds (if present). The result  $N_{pe}$  is the mean number of photoelectrons seen at the receiver. To evaluate signal detection capabilities of photoelectrons, background noise must be determined:

$$N_B = \frac{\eta_q}{h\nu} N_\lambda \lambda_{BP} \Omega_R A_R \eta_R \tau_{RG}$$

where  $N_\lambda$  is the background spectral radiance (night sky provides a best-case noise background of  $3 \times 10^{-6}$  W/ster m<sup>2</sup>, while sunlit clouds provide a worst-case noise background of  $1.4 \times 10^8$  W/ster m<sup>2</sup>),  $\Omega_R$  is the detector FOV solid angle in steradians,  $\lambda_{BP}$  is the width of the bandpass filter, and  $\tau_{RG}$  is the temporal width of the range gate.

$$\Omega_R = \left( \frac{\theta_{FOV}}{2} \right)^2$$

where  $\theta_{FOV}$  is the detector FOV half angle in radians. Thus, the probability of signal detection can be approached as follows; Since the photon detection follows the Poisson probability distribution, the probability per laser pulse of detecting  $m$  number of photons (where  $N$

is the average number of photoelectrons):

$$P(m, N) = \frac{N^m}{m!} e^{-N}$$

Then the probability of detecting one photon from the background noise, which is the false alarm probability:

$$P_{FA} = 1 - e^{-N_B}$$

The photon detection probability, which is the probability of detecting one photon from the background noise and actual signals, is:

$$P_{PD} = 1 - e^{-N}$$

Where  $N = N_{PE} + N_B$  is the total photoelectrons number. Finally, the signal detection probability, the probability of detecting a signal from the background noise, is:

$$P_{SD} = (1 - P_{FA}) P_{PD}$$

The analysis ensures that the selected CCR type and diameter comply with the functional and performance requirements of the mission and evaluates their performance within the ILRS (International Laser Ranging) network. It also includes atmospheric transmission losses, which account for factors like zenith angle and potential interference from cirrus clouds. Background noise levels are also considered as they are crucial for assessing the system's ability to distinguish the laser signal from ambient environmental noise. However, the described model for simulating CCR photon return does not consider velocity aberration. As the satellite is going to be in LEO, the higher orbital velocity might reduce photon return. Effects of velocity aberration are going to be investigated in a further analysis. Also, attitude errors are not being considered.

Using MATLAB, the Link Budget Analysis is implemented. The script integrates parameters from multiple ground stations within the ILRS networks, simulating slant ranges, atmospheric and cirrus transmittance and computing detection probabilities for each station. This is a technique used to measure the distance between the ground-based stations and our satellite. The code used calculates and saves the probability of detecting a signal from the satellite by the stations. A snippet of the code is shown in Listing 1. After defining the constants of the energy of a single photon at 532nm, CCR diameter, wavelength, reflectivity of the coated CCR, altitude (500km), background noise at night and day, the file containing the properties of each station is imported. Then, after defining the quantities mentioned in the formulae above, the final probabilities are calculated by two for loops ranging through 20° to 90°.

```

1 N_b_day = (data.n_q./hv).*N_bg_day.* (data.
    .lambda_bp.*1E-09).*omega_r.*A_r.*data.n_r
    .* (data.rangegate.*1E-09);
2 %noise photons (day)
3 N_b_night = (data.n_q./hv).*N_bg_night.* (data.
    .lambda_bp.*1E-09).*omega_r.*A_r.*data.
    n_r.* (data.rangegate.*1E-09);
4 %noise photons (night)
5
6 step = 1;
7 Ph = zeros(42,height(data));
8 P_PD = zeros(42,height(data));
9 P_SD_day = zeros(42,height(data));
10 P_SD_night = zeros(42,height(data));
11
12 for i = 90:-1:45
13     zen = deg2rad(90-i);
14     %zenith and incidence angle
15     R = height2range(alt_alba,data.Elevation,
16     i);
17     %slant range
18     theta_ref = asin(sin(zen)/1.455);
19     %internal refracted angle
20     mu = sqrt(1-(tan(theta_ref))^2);
21     eta_ocs = (2/pi)*(asin(mu)-(sqrt(2)*tan(
22     theta_ref))*cos(zen));
23     %cross section reduction factor
24     OCS = (eta_ocs^2)*ocs_peak;
25     %OCS for incidence angle
26     rng = (1/(4.*pi.*R.^2)).^2;
27     %two way space loss
28     T_c = exp(-0.14*(1.341*sec(zen))^2);
29     %one way cirrus loss
30     T_a = exp(-0.25.*1.2.*sec(zen).*exp(-
31     data.Elevation/1000)./1.2));
32     %one way atmospheric loss
33     Ph(step,:) = E_t.*n.*G_t.*A_r.*T_a.^2.*
34     T_c.^2.*OCS.*rng';
35     %link equation
36     N = Ph(:,:,)+N_b_day'; %total number of
37     photoelectron (day)
38     P_PD_night(step,:)= 1-exp(-Ph(step,:));
39     %prob of signal+noise detection (night)
40     P_PD_day(step,:)= 1-exp(-N(step,:));
41     %prob of signal+noise detection (day)
42     P_SD_day(step,:)= (1-P_FA_day').*
43     P_PD_day(step,:);
44     %prob of signal detection from noise (day
45     )
46     P_SD_night(step,:)= (1-P_FA_night').*
47     P_PD_night(step,:);
48     %prob of signal detection from noise (
49     night)
50     step = step+1;
51 end

```

**Listing 1:** Snippet of the Matlab Code.

Then, the efficiency of the CCRs for every station during day and night were calculated. Below, only the plots of the CCRs' efficiency during the day are shown, as the night-time efficiencies were consistently high due to reduced noise, making the day-time data more relevant for analysis. However, the values for night-time conditions are shown; in table [2] and in for the coated CCR, in table [3] for the uncoated CCR and in table [4] for the MRR. These correspond to the stations with the best (first), median (second) and worst (last) values of efficiency. Additionally, the plots for the uncoated CCRs have been omitted, as their performance was similar to that of the coated CCRs. The plots are shown with respect to  $\theta_{zen}$ . The ef-

**Table 2.** Efficiency of coated CCR Detection at night

Station \ $\theta_{inc}$	20°	40°	60°	80°
GRSM	1.00	1.00	1.00	1.00
KTZL	0.57	0.99	0.99	0.99
WETL	1.89e-5	1.41e-4	4.12e-4	6.67e-4

**Table 3.** Efficiency of uncoated CCR Detection at night

Station \ $\theta_{inc}$	20°	40°	60°	80°
GRSM	1.00	1.00	1.00	1.00
KTZL	0.63	0.99	0.99	0.99
WETL	2.25e-5	1.69e-4	4.9e-4	7.96e-4

ficiency for the coated CCR is shown in figure [5] and in [6] for the MRR.

A station is considered suitable for laser ranging if at any time detection probability per pulse exceeds 50% in a zenith angle range, for both night and daytime laser ranging. The stations used for this research are shown in Table 5. The plots above show the impact of the incident angle at a constant distance on the efficiency. The threshold line corresponds to 50% efficiency that is considered favorable. The night probabilities are generally be higher due to lower background noise, making it easier to distinguish the signal from the noise. The efficiencies of each CCR was then calculated in two situations and we acknowledged two cases; the ideal, where the satellite is exactly over the ground station and the worst, where the satellite is just over the horizon. These two cases correspond to the minimum and maximum distances. In the ideal case, the zenith angle is at 90° and the incident angle at 90°. In the worst case the zenith angle is 20° and the incident angle 60°. Regarding the efficiency for the worst case scenario for both day and night, the figures are shown in Figure 7 for the MRR and in Figure 8 for the coated CCR. The uncoated is omitted as it has similar performance.

The constant values in the plots could be due to specific characteristics or behaviors in the underlying calculations. The values of the probabilities are calculated based on the formulae mentioned before.

$$P_{PD} = 1 - e^{-N}$$

**Table 4.** Efficiency of MRR Detection at night

Station \ $\theta_{inc}$	20°	40°	60°	80°
ARKL	1.00	1.00	1.00	1.00
AREL	0.99	0.99	0.99	0.99
WETL	4.52e-4	3.39e-3	9.83e-3	0.01

<u>Stations</u>	<u>Location</u>	<u>Stations</u>	<u>Location</u>
JFNL	Wuhan, CN		
MATM	Matera, IT	SEJL	Sejong City, KR
POT3	Potsdam, DE	GMSL	Golosiv, UA
GRZL	Graz, AT	BEIL	Beijing, CN
GRSM	Grasse, FR	THTL	Tahiti, PF
SFEL	San Fernando, ES	HA4T	Haleakala, US
WETL	Wettzell, DE	MONL	Mon. Peak, US
ZIML	Zimmerwald, CH	GODL	Greenbelt, US
BORL	Borowiec, PL	YARL	Yarragadee, AU
HERL	Herstmonceux, GB	KTZL	Katzively, UA
SISL	Simosato, JP	IRKL	Irkutsk, RU
STL3	Mt Stromlo, AU	BADL	Badary, RU
SHA2	Shanghai, CN	ZELL	Zelenchukskaya, RU
KUN2	Kunming, CN	SVEL	Svetloe, RU
HRTL	Hartebeesthoek, ZA	BAIL	Baikonur, KZ
HARL	Hartebeesthoek, ZA	ARKL	Arkhyz, RU
BRAL	Brasilia, BR	RIGL	Riga, LV
SJUL	San Juan, AR	ALTl	Altay, RU
AREL	Arequipa, PE	MDVS	Mendeleev 2, RU
		SIML	Simeiz, UA

**Table 5.** Stations used and their locations.

for the detection of the signal and noise and:

$$P_{SD} = (1 - P_{FA}) \times P_{PD}$$

for the detection of signal from noise, where N is the total number of detected photons (including noise).  $P_{PD}$  is the probability of detecting both photons and noise,  $P_{SD}$  is the probability of detecting just noise and  $P_{FA}$  is the probability of false alarm. When the photon count N becomes very large, the expression of the exponential approaches zero, causing the probability to approach 1. So, the probability of detection becomes almost constant at 1, leading to a straight horizontal line. Conversely, if N is very small, the exponential is close to 1, making the probability close to 0. This also results in a constant value in the plot.

### 2.3 Orbit Determination - Orekit

OREKIT is a low level space dynamics library written in Java, released in 2008; it provides basic elements (orbits, dates, attitude, frames) and various algorithms to handle them (conversions, propagations, pointing). In our work, we use it for orbit propagation, frame transformations, attitude handling, orbit determination, event detection and data handling. The final result is an estimated orbit that best fits the observational data, as well as visualization of the results, showing how well the estimated orbit matches the observations and analyzes the errors in

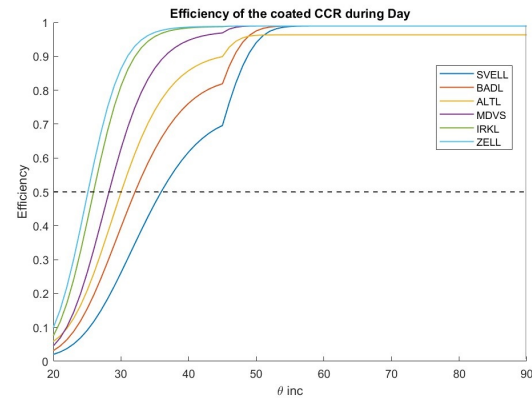


**Fig. 5.** Efficiency for the coated CCR.

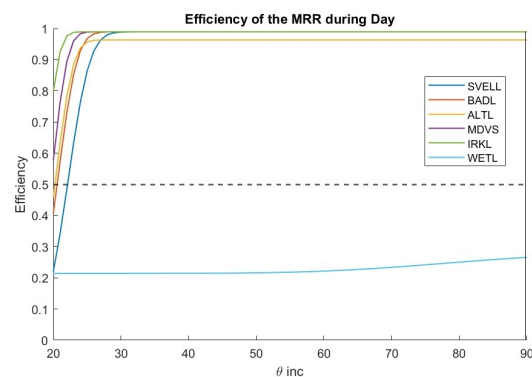


**Fig. 6.** Efficiency for the MRR.

the estimated parameters. More specifically, the steps we follow in the notebook are shown below in Algorithm .1 in pseudocode format.

### 3. iOTA

The In-Orbit Tumbling Analysis, iOTA, is a simulation tool developed by Hyperschall Technologie Goettingen GmbH and licensed under the ESA “Community” Licence, able to simulate the orbit and the laser tracking.

The software allows you to simulate the orbit of a specific spacecraft over long periods of time, considering all orbital disturbances, as other software does (e.g. GMAT). It also features the possibility of adding an observation campaign using laser tracking from ground stations to compare the position of the satellite calculated using the analytical approach, with that obtained with the simulated laser tracking.

For our specific case, a simplified CAD model of our 2U CubeSat has been created and imported on iOTA; then the 2 CCRs and the MRR were directly added inside the

---

**Algorithm .1:** Satellite Orbit Determination

---

**Data:** Satellite data (TLE, CPF, range measurements, etc.)  
**Result:** Enhanced orbit model, CPF file, validation plots

- 1 Step 1: Initialization and Setup;**
- 2 Initialize environment and libraries (Orekit, Python tools);
- 3 Define frames (ECI, ECEF, LVLH) and propagators (SGP4, numerical);
- 4 Load satellite data (TLE, CPF, mass, drag coefficient);
- 5 Step 2: Data Preparation;**
- 6 Process range measurement data from ground stations;
- 7 Set up observation model, estimator, and optimizer;
- 8 Step 3: Orbit Determination;**
- 9 Build numerical propagator with refined parameters;
- 10 Perform optimization to fit range measurements to estimated orbit;
- 11 Retrieve optimized orbit parameters;
- 12 Step 4: Propagation and State Retrieval;**
- 13 **foreach** time step in the propagation period **do**
- 14     Propagate satellite state using refined propagator;
- 15     Retrieve position and velocity vectors in ECI, ECEF, LVLH frames;
- 16     Compute differences with CPF and TLE data;
- 17     Store results;
- 18 **end**
- 19 Step 5: Visualization of Results;**
- 20 Plot delta position between CPF and estimated orbit in LVLH frame;
- 21 Plot delta position between original TLE, fitted TLE, and estimation in LVLH frame;
- 22 Step 6: TLE Fitting and Enhancement;**
- 23 Fit a new TLE to the refined orbit using optimization;
- 24 Adjust orbital elements and set BSTAR as a free parameter;
- 25 Step 7: Generate CPF File;**
- 26 Propagate orbit for 7 days and save in CPF format;
- 27 Export CPF file for laser ranging stations;
- 28 Step 8: Validation and Comparison;**
- 29 Re-propagate using fitted TLE;
- 30 Compare fitted TLE with initial TLE and refined orbit;
- 31 Visualize results to validate accuracy improvement;

---

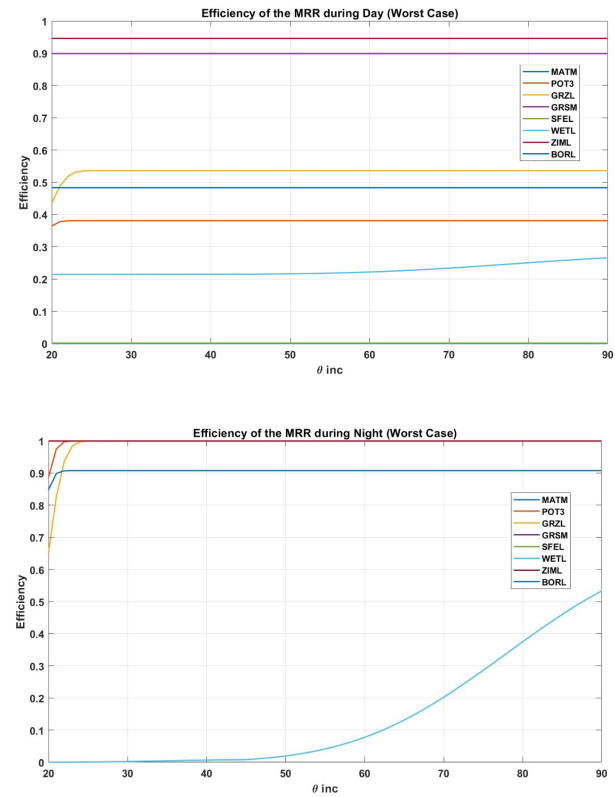


**Fig. 7.** Worst case efficiency for the MRR.

software (Table 6). At this point a simplification were made: due to the characteristics of iOTA itself, the minimum value of usable surface for a retroreflector is 0.001 m<sup>2</sup>, exceeding the area of our two smallest CCRs, around 0.0005 m<sup>2</sup>, however the approximation had minimal impact, considering the overall scope and level of the study.

#	Position	Surface reflectivity[-]	Reflector area[m <sup>2</sup> ]
CCR1	+y	0.93	0.001
CCR2	-y	0.78	0.001
MRR	-z	0.93	0.002

**Table 6.** Retro Reflectors

Subsequently, the orbital parameters, the most relevant orbital disturbances for our case, and the simulation time interval have been added, and two different kinds of simulations were then conducted:

- A 10-day simulation with the spacecraft fixed in the nadir pointing configuration, to represent the active phase of the satellite, when the Attitude Determination and Control Systems (ADCS) is active and compensate the disturbances (Fig.9);
- A 7-day simulation with the spacecraft free to tumble, to represent the inactive phase of the satellite,

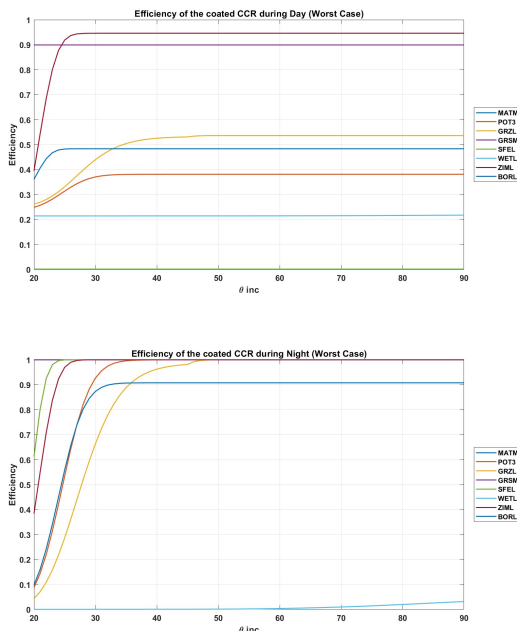


Fig. 8. Worst case efficiency for the coated CCR.

when it will be turned off after the mission, or will be dead for any reason (Fig.10).

*Note:* in the active phase the spacecraft's attitude was fixed instead of utilizing the ADCS section in iOTA, in order to simplify the program and reduce simulation time. Finally, 18 ILRS (International Laser Ranging Service) stations have been added, to carry out the laser ranging campaign. Only the European stations were considered, as they will probably be the only ones accessible when the spacecraft is in orbit.

Now the two different analyses results will be divided:

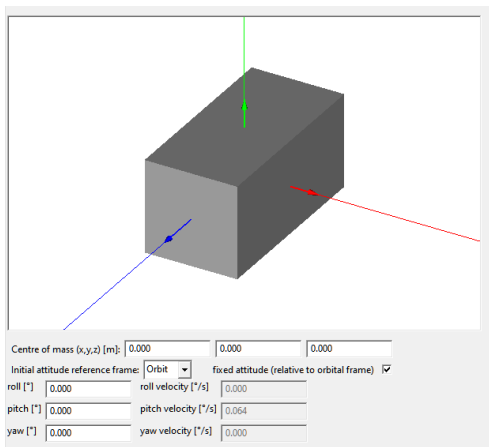


Fig. 9. iOTA fixed simulation configuration

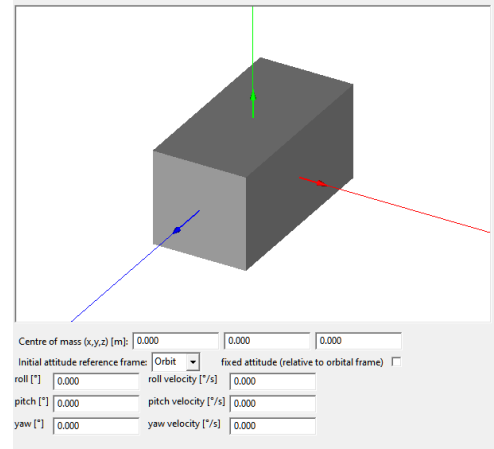


Fig. 10. iOTA free simulation configuration

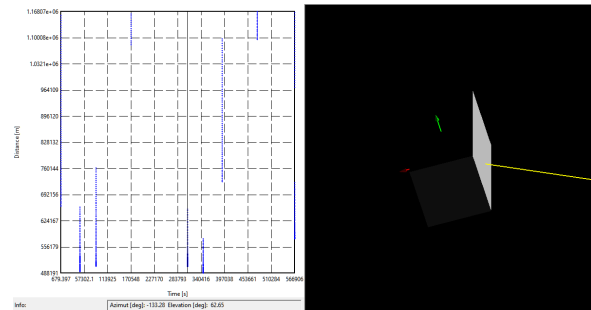


Fig. 11. Example of results obtained by the iOTA from a laser observation campaign, conducted from an ILRS station

### 3.1 Fixed Simulation

Due to the fixed attitude configuration used, in this case, the CCRs positioned on the lateral faces are rarely visible from all ILRS stations, while the third one (i.e. the MRR) is visible for time intervals consistent with the chosen orbit. In this case the attitude has not been determined, because, since the ADCS is active the nadir pointing configuration is ensured, while, if the ADCS is not active, we will refer to the second simulation. This simulation was still conducted to verify both the accuracy of the simulation parameters used and the reliability of the simulated laser range.

### 3.2 Free Simulation

In this case, given the freedom of movement of the spacecraft, all CCRs are more visible and multiple CCRs can be observed within a single observation period, with only a short time interval between reflections of various CCRs.

Since the orbit chosen for our satellite was very low, no sufficient tracking window to directly determine the atti-

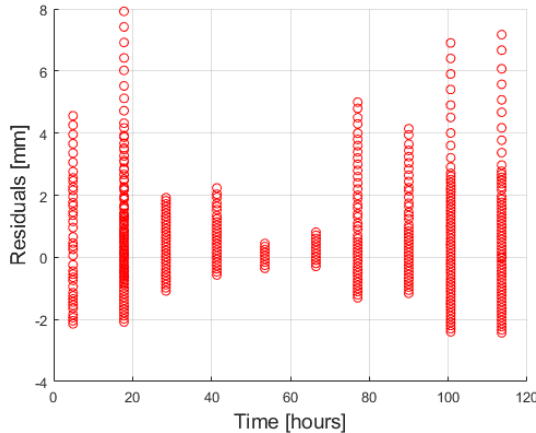


**Fig. 12.** Residuals from SIML station

tude has been obtained, as done by Sisi Zhao et al. [5]. Therefore, it was approximated with a different method. Specifically, the fact that the observed CCR is identifiable was exploited (thanks to the distinct far-field diffraction patterns given by the different coatings) and that the corresponding observation time and satellite velocity are known, and thus it is possible to determine the angular opening of observation; consequently, by exploiting the cases in which more than one CCR is visible during a laser beam measurement campaign, it is possible to obtain the same information for the subsequent mirror. Consequently, this could allow the derivation of the satellite's approximate spin period.

An example of the results obtained for each station is shown in Fig.12.

A more detailed and meaningful representation for a single observation window is provided in Figure 13.

The first dots on the left side of the diagram indicate the MRR residuals. The empty central section represents the non-reflective space between the two mirrors, while the last points on the right show the residuals determined by the reflection of the CCR on the +Y face.

Similar diagrams were obtained for each ILRS station, demonstrating the accuracy of the simulation.

#### 4. Data acquisition and processing

#### 5. Results

#### References

- [1] Daniel Arnold et al. "Satellite Laser Ranging to Low Earth Orbiters: Orbit and Network Validation". In: *Journal of Geodesy* 1-20 (Apr. 2018). DOI: 10.1007/s00190-018-1140-4.
- [2] Nils Bartels et al. "Design and qualification of a recessed satellite cornercube retroreflector for ground-based attitude determination via satellite laser ranging". In: Jan. 2020.

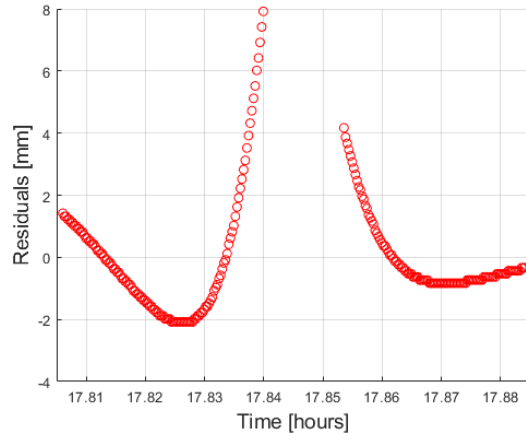


**Fig. 13.** Zoom of the residuals from SIML station

- [3] Mathieu Joerger et al. "Measurement error models and fault-detection algorithms for multi-constellation navigation systems". In: *IEEE/ION Position, Location and Navigation Symposium*. 2010, pp. 927–946.
- [4] John Degnan. "Millimeter Accuracy Satellite Laser Ranging: A Review". In: vol. 25. Jan. 1993, pp. 133–162. ISBN: 0-87590-526-9. DOI: 10.1029/GD025p0133.
- [5] Sisi Zhao et al. "Attitude analysis of space debris using SLR and light curve data measured with single-photon detector". In: *Advances in Space Research* 65.5 (2020), pp. 1518–1527. ISSN: 0273-1177. DOI: <https://doi.org/10.1016/j.asr.2019.12.005>. URL: <https://www.sciencedirect.com/science/article/pii/S0273117719308749>.
- [6] John Degnan. "A TUTORIAL ON RETROREFLECTORS AND ARRAYS FOR SLR". In: Nov. 2012.
- [7] Dariusz Strugarek et al. "Detector-specific issues in Satellite Laser Ranging to Swarm-A/B/C satellites". In: *Measurement* 182 (2021), p. 109786. ISSN: 0263-2241. DOI: <https://doi.org/10.1016/j.measurement.2021.109786>. URL: <https://www.sciencedirect.com/science/article/pii/S0263224121007399>.
- [8] Daniel Kucharski et al. "Attitude and Spin Period of Space Debris Envisat Measured by Satellite Laser Ranging". In: 52.12 (2014).
- [9] Georg Kirchner et al. "Determination of attitude and attitude motion of space debris, using laser ranging and single-photon light curve data". In: *Proceedings of the 7th European Conference on Space Debris, Darmstadt, Germany*. 2017, pp. 18–21.

- [10] Nicholas L Johnson. “Orbital debris: the growing threat to space operations”. In: *33rd Annual Guidance and Control Conference*. AAS 10-011. 2010.
- [11] John L Goodman. “History of space shuttle rendezvous and proximity operations”. In: *Journal of Spacecraft and Rockets* 43.5 (2006), pp. 944–959.
- [12] Mitsuhige Oda. “Experiences and lessons learned from the ETS-VII robot satellite”. In: *Proceedings 2000 ICRA. Millennium Conference. IEEE International Conference on Robotics and Automation. Symposia Proceedings (Cat. No. 00CH37065)*. Vol. 1. IEEE. 2000, pp. 914–919.
- [13] Nola Taylor Redd. “Bringing satellites back from the dead: Mission extension vehicles give defunct spacecraft a new lease on life-[News]”. In: *IEEE Spectrum* 57.8 (2020), pp. 6–7.
- [14] Robin Biesbroek et al. “The clearspace-1 mission: ESA and clearspace team up to remove debris”. In: *Proc. 8th Eur. Conf. Sp. Debris*. 2021, pp. 1–3.
- [15] Trupti Mahendrakar et al. “Real-time satellite component recognition with YOLO-V5”. In: *Small Satellite Conference*. 2021.
- [16] Anne Mergy et al. “Vision-based Neural Scene Representations for Spacecraft”. In: *Proceedings of the IEEE/CVF Conference on Computer Vision and Pattern Recognition*. 2021, pp. 2002–2011.
- [17] Timothy Philip Setterfield. “On-orbit inspection of a rotating object using a moving observer”. PhD thesis. Massachusetts Institute of Technology, 2017.
- [18] Antoine Petit, Eric Marchand, and Keyvan Kanani. “Vision-based space autonomous rendezvous: A case study”. In: *2011 IEEE/RSJ International Conference on Intelligent Robots and Systems*. IEEE. 2011, pp. 619–624.
- [19] Trupti Mahendrakar et al. “3D Reconstruction of Non-cooperative Resident Space Objects using Instant NGP-accelerated NeRF and D-NeRF”. In: *arXiv preprint arXiv:2301.09060* (2023).
- [20] Ben Mildenhall et al. “Nerf: Representing scenes as neural radiance fields for view synthesis”. In: *Communications of the ACM* 65.1 (2021), pp. 99–106.
- [21] Vassilis Karamanavis et al. “Characterization of deorbiting satellites and space debris with radar”. In: *Advances in Space Research* (2023).
- [22] Mitsuhige Oda, Kouichi Kibe, and Fumio Yamagata. “ETS-VII, space robot in-orbit experiment satellite”. In: *Proceedings of IEEE international conference on robotics and automation*. Vol. 1. IEEE. 1996, pp. 739–744.
- [23] JL Sch. “onberger and J.-M. Frahm,“Structure-from-motion revisited,””. In: *Proc. IEEE Conf. Comput. Vis. Pattern Recognit.* 2016, pp. 4104–4113.
- [24] Johannes L Schönberger et al. “A vote-and-verify strategy for fast spatial verification in image retrieval”. In: *Computer Vision–ACCV 2016: 13th Asian Conference on Computer Vision, Taipei, Taiwan, November 20–24, 2016, Revised Selected Papers, Part I* 13. Springer. 2017, pp. 321–337.
- [25] George N Guentchev et al. “Mechanical design and thermal analysis of a 12U CubeSat MTCW lidar based optical measurement system for littoral ocean dynamics”. In: *CubeSats and SmallSats for Remote Sensing V*. Vol. 11832. SPIE. 2021, pp. 71–98.
- [26] Wilfried Linder. *Digital photogrammetry: theory and applications*. Springer Science & Business Media, 2013.
- [27] Konrad Schindler. “Mathematical foundations of photogrammetry”. In: *Handbook of geomathematics*. Springer, 2015, pp. 3087–3103.
- [28] Francesco Capolupo and Pierre Labordette. “Receding-horizon trajectory planning algorithm for passively safe on-orbit inspection missions”. In: *Journal of Guidance, Control, and Dynamics* 42.5 (2019), pp. 1023–1032.
- [29] Sjoerd Van Riel. “Exploring the use of 3D GIS as an analytical tool in archaeological excavation practice”. In: (2016).
- [30] Chul-hong Kim, Tae-jae Lee, et al. “An application of stereo camera with two different FoVs for SLAM and obstacle detection”. In: *IFAC-PapersOnLine* 51.22 (2018), pp. 148–153.
- [31] Sabrina Corpino et al. “Space Rider Observer Cube – SROC: a CubeSat mission for proximity operations demonstration”. In: *73rd International Astronautical Congress*. 2022.
- [32] Luca Lion et al. “Kinematic tests on a docking mechanism for microsatellites”. In: *CEAS Space Journal* (July 2023). DOI: 10.1007/s12567-023-00516-w.